

RESEARCH ARTICLE

10.1002/2015WR017078

A pseudo genetic model of coarse braided-river deposits

Guillaume Pirot¹, Julien Straubhaar¹, and Philippe Renard¹

¹Centre for Hydrogeology and Geothermics (CHYN), University of Neuchâtel, Neuchâtel, Switzerland

Key Points:

- A new method is proposed to produce 3-D facies models of braided river aquifers
- The modeling method proposed integrates the use of analog data
- It produces a wide variety of realistic sedimentary structures

Correspondence to:

G. Pirot,
guillaume.pirot@unine.ch

Citation:

Pirot, G., J. Straubhaar, and P. Renard (2015), A pseudo genetic model of coarse braided-river deposits, *Water Resour. Res.*, 51, doi:10.1002/2015WR017078.

Received 11 FEB 2015

Accepted 16 NOV 2015

Accepted article online 22 NOV 2015

Abstract A new method is proposed to produce three-dimensional facies models of braided-river aquifers based on analog data. The algorithm consists of two steps. The first step involves building the main geological units. The production of the principal inner structures of the aquifer is achieved by stacking Multiple-Point-Statistics simulations of successive topographies, thus mimicking the major successive flooding events responsible for the erosion and deposition of sediments. The second step of the algorithm consists of generating fine scale heterogeneity within the main geological units. These smaller-scale structures are generated by mimicking the trough-filling process occurring in braided rivers; the imitation of the physical processes relies on the local topography and on a local approximation of the flow. This produces realistic cross-stratified sediments, comparable to what can be observed in outcrops. The three main input parameters of the algorithm offer control over the proportions, the continuity and the dimensions of the deposits. Calibration of these parameters does not require invasive field measurements and can rely partly on analog data.

1. Introduction

In alpine regions such as Switzerland, water for drinking, irrigation or industrial purposes is frequently tapped from gravel braided-river aquifers [FOEN, 2009]. To understand, manage and protect groundwater resources in this type of system, and/or to better model aquifer-river interactions at multiple scales, models of internal geological heterogeneity are required. These models can be used, for example, to assess the uncertainty of contaminant migration within such aquifers. In a previous paper [Pirot *et al.*, 2014], we proposed to model the evolution of braided-river topographies using LIDAR data from analog sites and multiple-point statistics. In this paper, we build on this idea and consider the internal geological architecture of braided systems.

To constrain our model, we rely on a vast literature that describes the geology of braided systems. Braided rivers are composed of multiple channels that intersect successively, producing braid patterns [Leopold *et al.*, 1957; Howard *et al.*, 1970]. The sediments transported and deposited by these active systems are mainly sand and gravel [Williams and Rust, 1969; Miall, 1977; Siegenthaler and Huggenberger, 1993; Huggenberger and Regli, 2006]. Some finer grain size sediments such as silt or clay may be observed at the surface of an active system after flow recession or vegetation retention, but are generally not as well preserved in the recorded deposits [Huber and Huggenberger, 2015a] due to the high energy of such systems [van der Nat *et al.*, 2002]. The classification of braided-river components [Allen, 1983; Miall, 1985; Labourdette and Jones, 2007] provided an essential nomenclature (channel, gravel bars, bedforms) for the description and analysis of such systems. Length-scale characterization studies [Sapozhnikov and Fofoula-Georgiou, 1996; Fofoula-Georgiou and Sapozhnikov, 2001; Hundey and Ashmore, 2009] have revealed self-affinity and scale invariance in the geomorphology of braided rivers. Detailed outcrop analyses [Klingbeil *et al.*, 1999; Labourdette and Jones, 2007; Bayer *et al.*, 2011] and ground-penetrating radar measurements and interpretations [Huggenberger, 1993; Bridge *et al.*, 1995; Lunt and Bridge, 2004; Huber and Huggenberger, 2015b] have reinforced the knowledge of sedimentary structures and heterogeneity in braided-river aquifers. According to Huber and Huggenberger [2015b], essential features of braided-river aquifers may be attributed to a layering of successive gravel sheets eroded by scours and then filled with cross-stratified deposits.

General understanding of the dynamic processes occurring in braided rivers has been improved through on-site process description [Rust, 1972; Ashworth *et al.*, 1992; Jones and Schumm, 2009], planform and morphological evolution analyses [Ashworth, 1996; Lane *et al.*, 2003; Brasington *et al.*, 2012], granulometry and

bed-load transport studies [Ashmore, 1988; Dawson, 1988; Surian, 2002] and a wide variety of flume experiments [Ashmore, 1982; Kleinhans and Brinke, 2001; Van De Lageweg *et al.*, 2013]. Derived from physical laws, flow and sediment-transport models have been developed [Fredsoe, 1978; Ashworth *et al.*, 1994; De Serres *et al.*, 1999; Dargahi, 2004; Millar, 2005; Davy and Lague, 2009]. These physically based models, along with cellular automata models [Murray and Paola, 1994; Coulthard *et al.*, 2002; Thomas and Nicholas, 2002], take into account the transport of sediments on the surface topography and sometimes other processes such as avulsion [Jerolmack and Paola, 2007] or the interaction with vegetation [Edwards *et al.*, 1999; Murray and Paola, 2003; Thomas *et al.*, 2007]. They allow us to analyze the evolution of the surface morphology of braided rivers but they do not provide the resulting internal structure and heterogeneity of the subsurface.

All of the above conceptual and process-based knowledge has allowed researchers to build various kinds of structure-imitating models of the internal heterogeneity of braided-river aquifers, with the aim of better understanding the control of heterogeneity on solute or contaminant transport [Boggs *et al.*, 1993; Rodgers *et al.*, 2004]. The simplest models are based on traditional multi-Gaussian geostatistics [Felletti *et al.*, 2006; Salamon *et al.*, 2007; Glenz, 2013] or indicator simulation [Klise *et al.*, 2009]. More realistic three-dimensional models of geological heterogeneity can be generated by pseudo-genetic, object-based and multiple-point geostatistical methods. Webb [1994] was one of the first to propose a process-imitating method to produce models of geological heterogeneity for braided-river aquifers. This approach is based on the vertical stacking of successive topographies of the braided river simulated by random walks [Webb, 1995]. One limitation of this method is that, aside from channel width and depth, all surfaces between channels are considered as flat. The method has been used by Anderson *et al.* [1999] to model hydrogeological properties of a braided-stream deposit and has been tested on a groundwater flow and transport problem. Teles *et al.* [2001] proposed an agent-based model allowing the description of a fluvial system at a rather large scale. The processes of erosion and deposition were simulated using a set of simple rules and a multiagent system. Using this framework, and providing paleo information about the flow and sediment load in the fluvial plain over time scales of some thousands of years, the model allowed for the reconstruction of heterogeneity structures in 3-D. Recently, stochastic object-based models have been developed for braided rivers [Ramanathan *et al.*, 2010; Huber, 2015]. These algorithms are computationally efficient when no conditioning to field data is required. Comunian *et al.* [2011] proposed an innovative way, based on multiple-point statistics [Straubhaar *et al.*, 2011], to model a 3-D braided-river deposit from sedimentological observations on a series of seven cross sections collected at the Herten site in Germany by Bayer *et al.* [2011]. This method proved the ability of MPS to reproduce complex fine-scale geological structures, but the available data in this case only allowed modeling of a rather small area (16 m × 10 m × 7 m).

In this paper, a new pseudo-genetic algorithm is proposed. The method revisits the principles established by Webb [1994]. It is based on the stacking of successive topographic simulations to create geological units, within which geological facies or geophysical properties can be assigned. The proposed-algorithm is hierarchical and involves two levels of simulation as well. At the first level, the main geological units of the braided-river aquifer are simulated as successive deposits, as a result of successive major flood events that are able to mobilize gravel sheets and form scours. At the second level, *i.e.*, within each geological unit, scours are filled by cross-bed deposits caused by local flow conditions and sediment sorting. Novelties of this work involved the way in which the successive topographic simulations are produced as well as the way in which the geological facies are assigned. The topographies are simulated with the method developed by Pirot *et al.* [2014], which is based on the Direct Sampling Multiple-Point Statistics (MPS) algorithm [Mariethoz *et al.*, 2010]. This provides not only a realistic topography of the channels, but also of the bars and islands. Furthermore, the temporal evolution of the topography is also modeled using multivariate MPS. Then the assignment of the geological facies is not based on an estimation of the Froude number as done by Webb [1994], but on a deformation process that mimics a repeated facies sequence, producing cross-bedded deposits. The approach is illustrated with a training data set composed of successive DEMs of the Waimakariri River, New Zealand [Lane *et al.*, 2003] acquired with LIDAR at four time steps.

The paper is organized into two main parts. The first part (section 2) presents the methodology used to build heterogeneity models of braided-river aquifers. Section 2.1 gives an overview of the pseudo-genetic algorithm and its global parameters. The method to produce successive MPS simulations of topographies conditional to the previous topographic surface and the way of stacking these topographies to build a geological layer are detailed in section 2.2. Then, the generation of facies heterogeneity within the geological

layers is presented in section 2.3. In the second part of the paper (section 3), the resulting models are presented (section 3.1). These are compared to field outcrops (section 3.2). A sensitivity analysis of the algorithm to its main input parameters is presented in section 3.3. Recommendations to determine the parameters are suggested in section 3.4.

2. Methodology

2.1. Algorithm and Main Parameters

The general outline of the proposed algorithm is presented in Algorithm 1 and its principles are described thereafter. The initialization consists in producing an initial topography that will constitute the bottom of the aquifer, using the Direct Sampling MPS algorithm [Mariethoz *et al.*, 2010]. Then successive iterations follow until the aquifer model reaches the desired thickness. Knowing the previous topography, the next one is simulated using MPS conditionally to the previous one, as described in detail in Pirot *et al.* [2014]. The next topography is then stacked over the previous one with an aggradation rate fixed for all iterations (Table 1). The new topography partly erodes the underlying layers and deposits sediments that constitute a new geological layer. If the resulting aquifer model does not reach the desired thickness, the algorithm's loop continues, else it stops. Facies heterogeneity is generated within the geological layers by simulating in a simplified manner the formation of cross-beds within the troughs.

The algorithm uses parameters at two levels (see Table 1). The first level parameters describe the dimensions of the model and are required to build the main structures—the geological layers—of the model. The second level ones are used to generate heterogeneity within the geological layers. Three main parameters offer a control on the geometry and the dimensions of the geological structures generated by the algorithm: the aggradation rate α , the flow power f_p and the number of intra-layer iterations n . Then scaling factors allow the user to stretch or shrink the model in order to fit characteristic length scales. The aggradation rate α represents the thickness of the deposited geological layers. The flow power f_p is linked to the energy of the system and to the thickness of the cross-stratified deposits in the scours while the number of intra-layer iterations n is related to the number of cross-stratified deposits in the scours.

This approach assumes that aggradation takes place during large flood events that remodel the topography of the river. Indeed aggradation requires an input of sediments greater than the sediment discharge

Algorithm 1: pseudo genetic algorithm for three-dimensional facies heterogeneity models of braided-river aquifers

```

1: procedure brahms (parameter file)
2:   simulate initial (bottom) topography
3:   initialize current model thickness  $\leftarrow 0$ 
4:   while current model thickness < desired thickness do
5:     simulate next topography conditionally to the previous topography
6:     stack the next topography over the previous topography to build a geological layer
7:     subtract the induced erosion to the underlying layers
8:     generate geological heterogeneity within the new geological layer
9:     compute the current model thickness
10:    set the previous topography  $\leftarrow$  next topography
11:  end while
12:  return 3D heterogeneous facies model
13: end procedure

```

Table 1. Main Parameters

Main Parameters	Name	Value
<i>Large-Scale Structural Parameters</i>		
zone of interest aquifer model parameters	length (flow direction)	200 m
	width (orthogonal to the flow direction)	100 m
	minimum thickness - depth	12 m
	cell length	2 m
	cell width	2 m
	cell height	0.1 m
braided-river topography dimensions	length	11,600 m
	width	1,200 m
	cell length	20 m
	cell width	20 m
interpolation parameters	margin length	5 m
	margin width	5 m
	margin depth	0 m
	scaling factor along length axis	1
	scaling factor along width axis	1
	scaling factor along depth axis	1
facies parameters	coarse grain size sediment facies value	1
	medium grain size sediment facies value	2
	fine grain size sediment facies value	3
	default value	0.3 m/geological layer
<i>aggradation rate α</i>		
<i>Small-Scale Parameters</i>		
iterative deformation parameters	number of iterations n – default value	6
	facies sequence – default sequence	[3; 1; 3; 1; 3; 1; 2]
	flow power f_p – default value	5
	smoothing radius r	3

[Germanoski and Schumm, 1993] and it generally occurs during large flood events [Google-Images, 2015]. At a field site, it is very difficult to know precisely what part of the sediments has been mobilized and transported or remodeled during a flood. So at a specific location, an observed aggradation after a large flood event does not mean that no erosion occurred below the surface that constituted the topography before the flood. To produce the main geological structures, the method assumes that the structures of the successive deposits are largely influenced by the evolution of the surface topography of braided-rivers. In other words, the erosion surfaces that define unit interfaces in the recorded geology are supposed to be similar to visible topographies.

Field observations of actual active braided-river systems often do not show significant aggradations. Some detailed studies [Lane et al., 2003] show only some cyclic evolution of braided-river geomorphology. Though gauging stations provide information about flood frequency and magnitude, they do not allow to link these clearly with the aggradation rate [Sambrook Smith et al., 2010]. In addition, braided-river system outcrops do not show significant changes or trends in the dimensional characteristics of the deposits at one location. This medium to large scale stationarity of the deposit dimensions can be compared to the braided-river self-affinity described by Sapozhnikov and Fofoula-Georgiou [1996]. Therefore in absence of more specific information, it has been decided to keep the aggradation rate fixed in the algorithm for the moment. Note, however, that a more sophisticated distribution of the aggradation quantities over time can easily be handled by the proposed modeling framework.

The parameters have to be adjusted and inferred from field observations. Outcrop analysis, ground penetrating radar (GPR) section interpretations, borehole data or analog sites shall provide information about the thickness of the main geological layers and therefore about the aggradation rate, as well as characteristic dimensions of the deposit structures and facies proportions and properties.

2.2. Building the Main Depositional Structures

The main depositional structures or geological layers are obtained sequentially by stacking together successive simulations of digital elevation models (DEMs). In order to produce successive topographies that are coherent with the successive river topographic patterns, DEMs are generated at a scale at least as large as the river width [Pirrot et al., 2014], which might be larger than the zone of interest. This is why there are two kinds of simulation grid as described in Table 1. A three-dimensional simulation grid is defined for the zone

of interest and a two-dimensional simulation grid is defined for the DEMs simulations. The length and width of this latter shall be greater or equal to the length and width of the zone of interest. As the resolution of these two grids might differ, interpolation parameters (see Table 1) allow rescaling of the extracted zone of the simulated topographies to the zone of interest. It might also be used to update the analog length scale characteristics if necessary.

2.2.1. Simulation of Successive Topographies

The first step consists in producing sequentially successive topographies of a braided-river according to the method described in detail by *Pirot et al.* [2014]. The method uses a set of LIDAR images at different time steps showing the evolution of the topography of the river bed such as the four successive images of the Waimakariri river [*Lane et al.*, 2004]. Other sources of successive DEMs such as LIDAR data taken at other locations or topographies computed with a physically based model of erosion and deposition could be used as well as training set. From these data, the Direct Sampling algorithm simulates the new topography (time step t) conditionally to the previous one (time step $t - 1$). The algorithm uses the statistical relations between the topographic patterns in the two successive topographies measured in the field and reproduces them in the simulation. This ensures, for example, that a given channel may migrate at a reasonable distance or vanish between two successive simulations following what has been observed in the analog data set.

Here the method is applied on a grid of size $11,600 \text{ m} \times 1,200 \text{ m}$, as indicated in the braided-river topography dimension parameters of Table 1. The parameters to run the Direct Sampling algorithm in order to produce the topography time series are described in detail in *Pirot et al.* [2014]. The result of four successive topography simulations are displayed in Figure 1a).

Then, in absence of specific information about the location of the zone of interest, this latter is randomly retrieved so that all pixels within it are in the domain of the large scale topography simulation grid. The location of the zone of interest is the same for all the successive topographies. This extraction step takes into account the different scaling factors (see Table 1) that allow stretching or shrinking the topographies along the model axis to adapt the characteristic length scale (channel width, bar dimensions. . .) of the analog to the characteristic length scale of the site to model. Due to the possible different grid resolutions of the braided-river topography simulations (coarser scale) and the aquifer geological model (finer scale), margin parameters are used to extend the zone of interest, which allow for a better interpolation of the topography at the aquifer model scale. The extracted topography is interpolated linearly on the aquifer model grid. Though more advanced interpolation techniques like splines could have been considered, the use of a linear interpolation was deemed sufficient since the resulting surfaces were reasonably smooth (see Figure 3).

2.2.2. Stacking Topographies to Create Erosion and Deposit Volumes

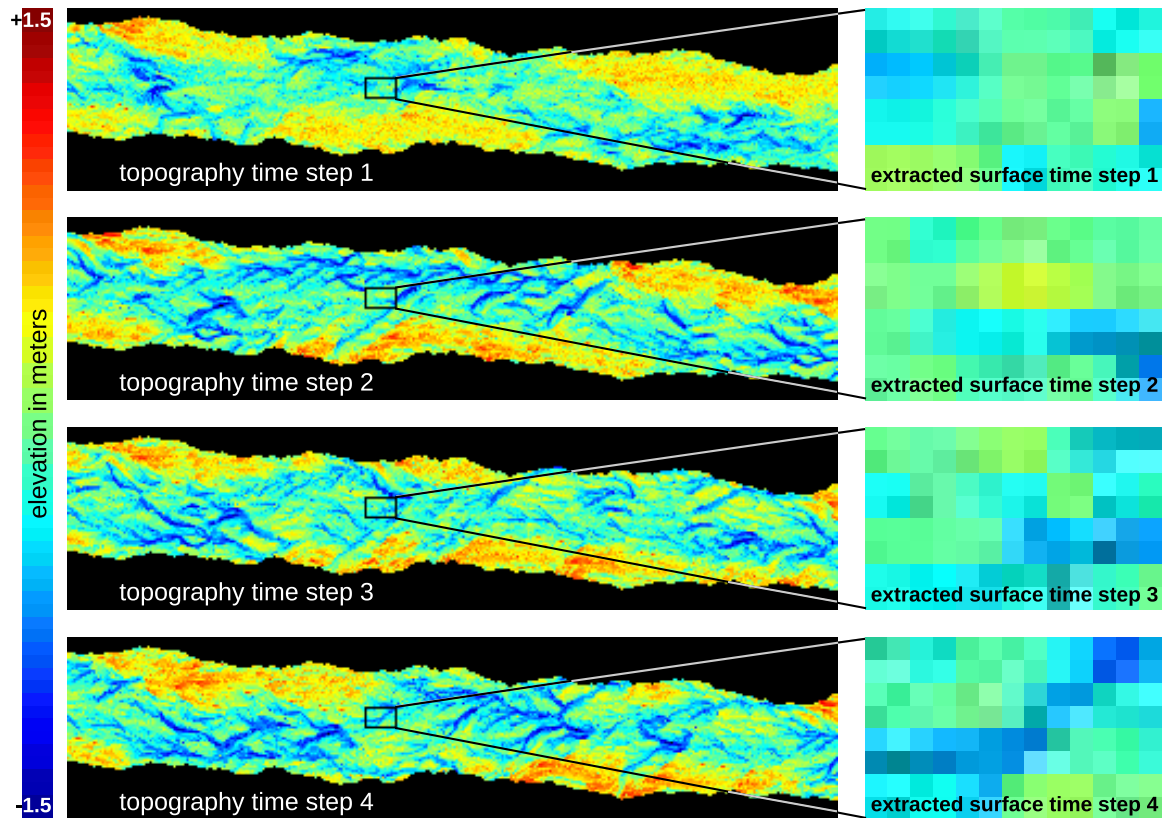
Now that a series of successive topographies is available, it is possible to stack them with a vertical increment, i.e., the aggradation rate α that is constant throughout the algorithm. As illustrated on a two-dimensional fictive section in Figure 1b), this process produces some erosion volumes and some deposition volumes. A positive aggradation rate allows building a succession of geological layers that reach a minimum given thickness for the simulated aquifer.

More precisely, let us denote by t each time step iteration and $(E_t)_{t \in \mathbb{N}}$ the ensemble of successive DEMs simulated by MPS. The ensemble of centered elevations $(C_t)_{t \in \mathbb{N}}$ are then defined as $C_t = E_t - \mu(E_t)$, $\forall t \in \mathbb{N}$, where $\mu(E_t)$ is the mean of E_t . Let us denote $(Z_t)_{t \in \mathbb{N}}$ the elevation of the surfaces delimiting the geological layers. The t^{th} geological layer G_t is delimited at the bottom by Z_{t-1} and at the top by Z_t . The bottom of the aquifer model Z_0 is initialized with C_0 . Then, sequentially, for each time step iteration t , the elevation of the top of the next main layer is computed as a function of the previous mean elevation and the aggradation rate: $Z_t = \mu(Z_{t-1}) + \alpha + C_t$. Additionally, the resulting erosions may impact all the previous elevations that need to be updated: $Z_p = \min(Z_p, Z_t)$, $0 \leq p \leq t-1$. The resulting elevations $(Z_t)_{t \in \mathbb{N}}$ are stored as a pillar grid. Once the main geological layers are defined, it is possible to define heterogeneous physical properties or facies within each layer.

2.3. Generate Geological Heterogeneity Within the Layers

The method presented hereafter to generate heterogeneous facies within the main geological layers is inspired by field observations of outcrops, processes, and studies linking surface topography with ground penetrating radar (GPR) measurements [*Huber*, 2015]. During a flood event and looking at the intra-layer scale, sandy gravel sheets are moving forward, filling progressively the scours formed by erosion at channel

a) Realizations of four successive topographies



b) Stacking two successive topographies

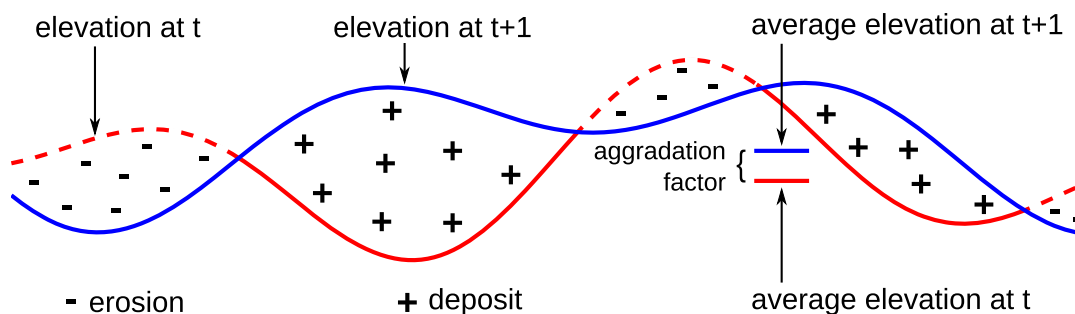


Figure 1. (a) Four successive topography realizations, followed by extraction and interpolation; (b) pseudo processes of erosion and deposit.

confluences [Rust, 1972]. When a gravel sheet collapses while moving forward over a scour, a granulometric sorting occurs. By gravity, coarse grain size materials are deposited first, followed by finer grain size sediments. With the combined action of the flow, this process produces cross-stratified deposits that can be observed in gravel-pits [Heinz et al., 2003].

To mimic this process and obtain stratified deposits, the bottom topography of a given layer is iteratively shifted and deformed locally, in accordance with local flow and topography constraints. Each iteration i defines a deposition volume for a distinct facies. The sequence of the facies is defined in Table 1. Within the framework of a sand and gravel braided river, it is assumed that three main facies types are sufficient to reproduce the main heterogeneity patterns. The three facies are differentiated according to their granulometry and sorting: facies 1 represents well sorted fine grain sediments, facies 2 represents unsorted mixed size sediments and facies 3 represents well sorted coarse sediments. Facies 2 can be interpreted as a low

permeability medium, representing heterogeneity within gravel sheets. Facies 1 and 3 represent the sorted sediments whose iterative successions form cross stratifications.

To shift and deform the topography, we first evaluate the direction in which the sediments should move. This is given by a rough approximation of the possible river flow direction that is described in section 2.3.1. Then, we also consider the orientation of the local slope since scour filling is oriented along the local flow direction and occurs at the edges of gravel sheets, where they can collapse. The same local flow conditions are used for all iterations within a geological layer. However, the downward slope is updated at each iteration. The deformation process is detailed in section 2.3.2.

In what follows, the processes to generate fine scale heterogeneities within the geological layers are explained for the t^{th} geological layer G_t which is delimited at the bottom and at the top by the Z_{t-1} and Z_t surfaces respectively, $\forall t \in \mathbb{N}^*$. Note that, within each geological layer $G_t, \forall t \in \mathbb{N}^*$, we assume that the generated geological heterogeneities are intrinsic to the layer: no erosion below the bottom of the layer or deposit over the top of the layer is created by this process.

2.3.1. Surface Flow Approximation

For each layer G_t , the flow approximation is computed from surface Z_{t-1} delimiting the bottom of the layer on a wider area than the zone of interest to avoid boundary effects and to take into account the global flow scale, which ensures a continuity at the local scale. So the flow is approximated on a grid of the same dimensions ($11,600 \text{ m} \times 1,200 \text{ m}$) as the one used to generate the successive topographies.

First, an against-current fast-marching method [Cao and Greenhalgh, 1994; Sethian, 1996, 1999] is applied on a velocity field v_{t-1} derived from the topographic surface Z_{t-1} to compute the travel time tt_{t-1} from any point on the river topography to the downstream outlet of the river, using a Matlab implementation developed by Peyré and Cohen [2006]. The downstream outlet is composed of all points of the topographic line corresponding to the right edge on Figure 2a). To compute this travel time, the topography Z_{t-1} is interpreted as a velocity field, with small velocity values at high elevations and greater velocity values at lower elevations. The velocity field used to compute this approximate travel time is defined as $v_{t-1} = -Z_{t-1} + 1.1 \times \max(Z_{t-1})$ to ensure strictly positive values.

Then the approximated flow field \widehat{F}_t within the t^{th} geological layer is computed as the opposite of the gradient of the travel time tt_{t-1} divided by its squared norm (see equation (1)).

$$\widehat{F}_t = - \frac{\overrightarrow{\text{grad}}(tt_{t-1})}{\|\overrightarrow{\text{grad}}(tt_{t-1})\|^2} \quad (1)$$

This method produces a flow map following the channel orientations and whose norm is slightly bigger in the channels, as displayed in Figure 2a).

It is important to note that this flow map does not pretend to be accurate. It is used only to get a rough approximation of the flow directions that can be computed very rapidly. More sophisticated calculations could be used as well but this was deemed not necessary at this point of the research.

2.3.2. Iterative Deformation Scheme

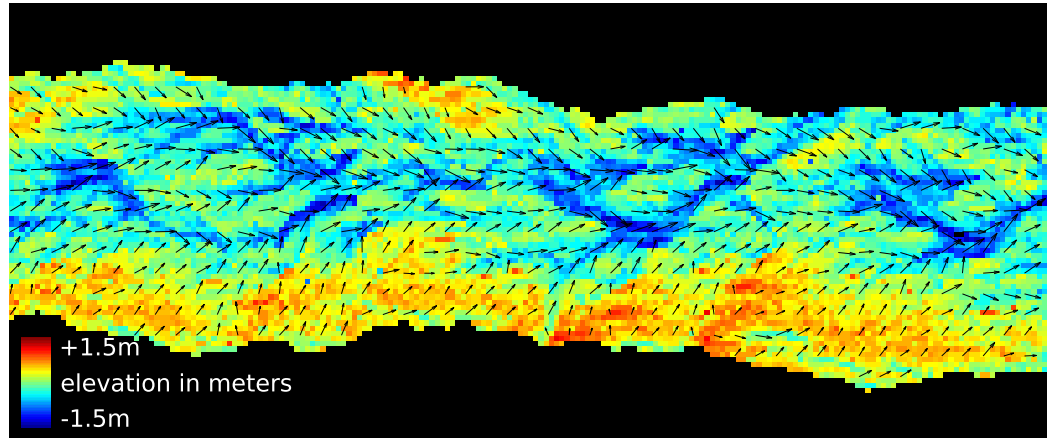
The number of iterations n within a geological layer as well as the facies sequence are defined in Table 1.

Within the t^{th} geological layer, all iterations use the same flow map $\widehat{F}_t = (v_x, v_y)^T$. It is assumed constant within the layer so that the deformations are progressive and smooth to produce cross-stratifications. The intensity of the flow might be adjusted with the flow parameter f_p . At each iteration $i, 1 \leq i \leq n$, the gradient $\overrightarrow{\text{grad}}(T_i) = (-u_i^x, -u_i^y)^T$ of the current topography T_i is computed. $T_0 = Z_{t-1}$ denotes the bottom and $T_{n+1} = Z_t$ the roof of the t^{th} geological layer. The deformation and shifting $\overrightarrow{d_{i+1}}$ is computed as a vector of scalar products (see equation (2)) constrained by co-directionality: opposite flow and downward slope direction cannot generate a sorted deposit and therefore cannot shift the topography.

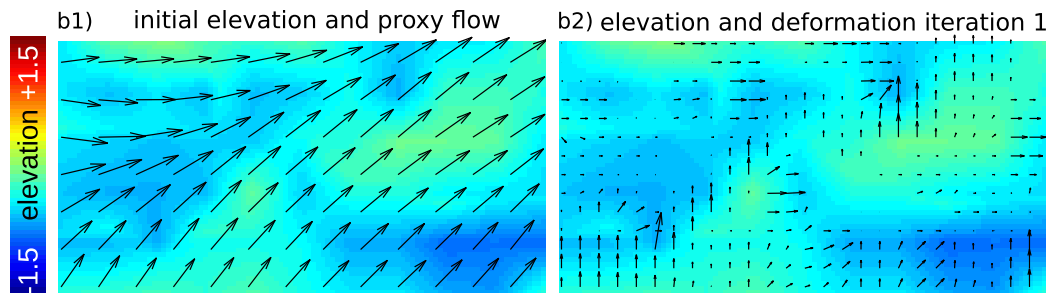
$$\overrightarrow{d_{i+1}} = f_p \cdot \begin{pmatrix} -\min(u_i^x, 0) \cdot \min(v_x, 0) + \max(u_i^x, 0) \cdot \max(v_x, 0) \\ -\min(u_i^y, 0) \cdot \min(v_y, 0) + \max(u_i^y, 0) \cdot \max(v_y, 0) \end{pmatrix} \quad (2)$$

The deformation $\overrightarrow{d_{i+1}}$ is applied to the coordinates $(X_i, Y_i)^T$ of the current topography T_i . The new coordinates $(X_{i+1}, Y_{i+1})^T = (X_i, Y_i)^T + \overrightarrow{d_{i+1}}$ are used to compute the next smoothed and shifted topography ST_{i+1}

a) Approximation of the global flow over the topography at the river scale



b) Iterative topography deformations at the zone of interest dimensions



c) Geological layer intrinsic iterative deformations and facies assignment

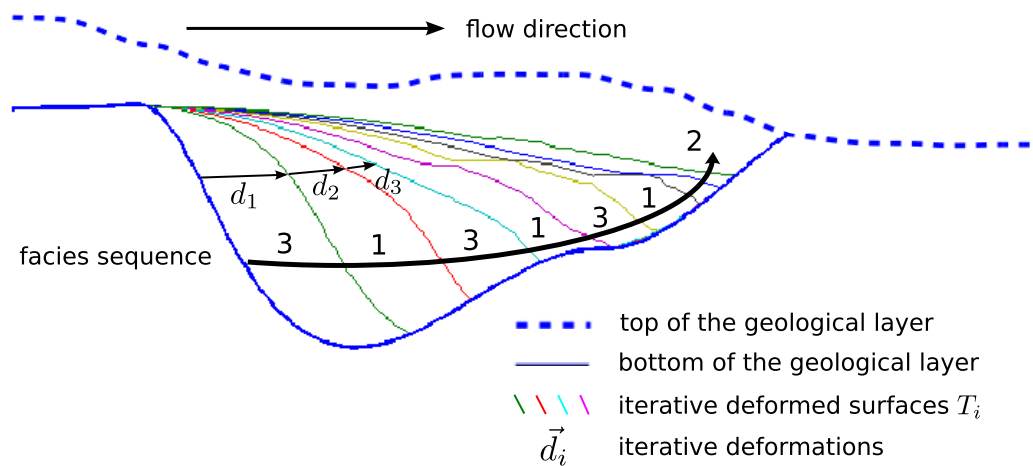


Figure 2. Flow approximation, iterative deformations and facies assignment.

(within the current layer) through a nearest neighbor interpolation followed by a moving average whose parameters are defined in Table 1: $ST_{i+1} = smoothInterpolation(X_{i+1}, Y_{i+1}, T_i)$. The topography T_{i+1} is constrained to be below the top topography T_{n+1} of the current layer, and as no erosion is desired, it is also limited by the value of the previous topography T_i : $T_{i+1} = \min(T_{n+1}, \max(T_i, ST_{i+1}))$. Figure 2b) provides an illustration of one iteration of these successive deformations, starting from an initial topography and a flow map. The facies assigned to the volume comprised between T_{i-1} and T_i is the i^{th} facies of the sequence. The remaining volume in the geological layer after n iterations, located between T_n and T_{n+1} – denoting the

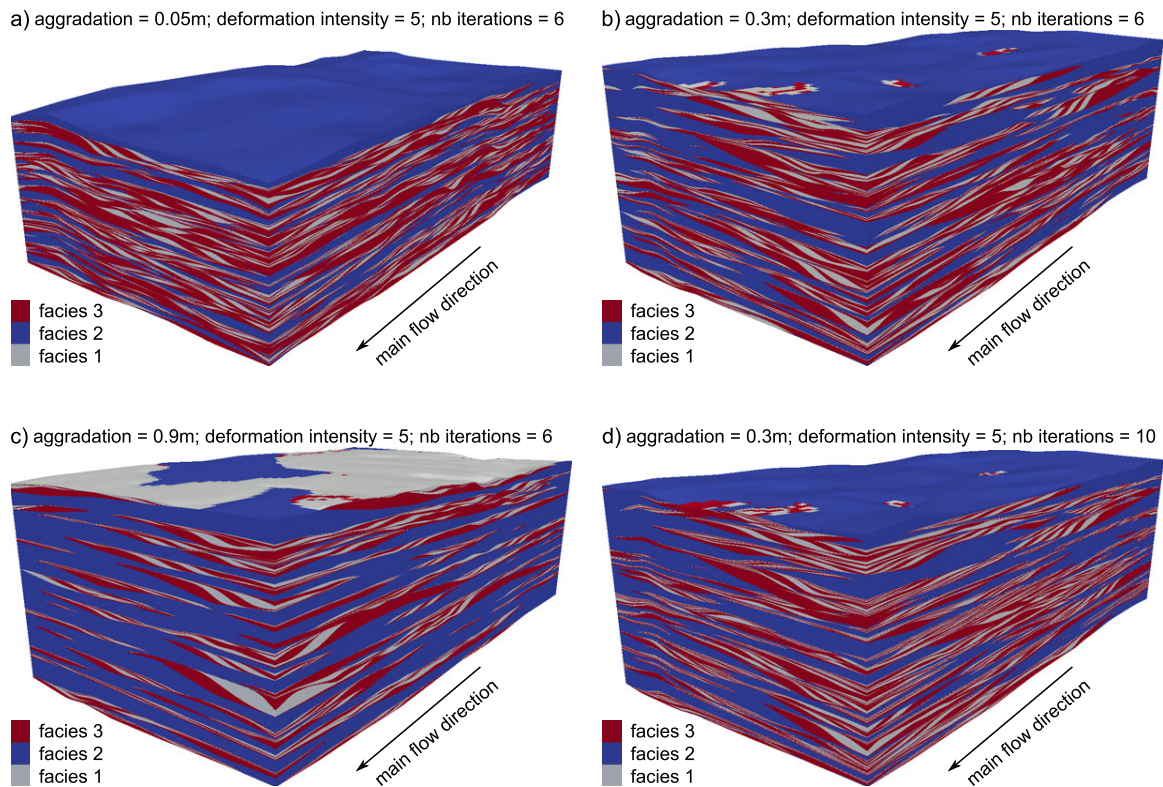


Figure 3. 3-D heterogeneous facies model (a) for an aggradation $\alpha = 0.05$ m, $n = 6$ inner-layer iterative deformations and a deformation intensity corresponding to a flow power $f_p = 5$; (b) for an aggradation $\alpha = 0.3$ m, $n = 6$ inner-layer iterative deformations and a deformation intensity corresponding to a flow power $f_p = 5$; (c) for an aggradation $\alpha = 0.9$ m, $n = 6$ inner-layer iterative deformations and a deformation intensity corresponding to a flow power $f_p = 5$; (d) for an aggradation $\alpha = 0.3$ m, $n = 10$ inner-layer iterative deformations and a deformation intensity corresponding to a flow power $f_p = 5$.

roof of the geological layer, is assigned the $(n + 1)^{th}$ facies of the sequence. According to the facies sequence defined in Table 1, facies 3 and 1 are alternatively assigned to the volumes delimited by the successive intermediate surfaces T_i , $i \in \{0, \dots, n\}$ and facies 2 is assigned in the remaining volume of the geological layer.

3. Results

3.1. Resulting Heterogeneity

As all topographies within each geological layer are generated over a regular grid, the resulting 3-D model can be stored as a regular pillar grid. Each layer of the model provides thickness and facies information at all locations of the regular horizontal grid.

Three examples of the resulting models using different aggradation rate α , flow power f_p and number of iterations n are presented in Figure 3. For further applications requiring a regular grid, the 3-D model is also discretized onto a 3-D regular grid whose cell dimensions are define in Table 1. An arithmetic mean is used for properties such as porosity or horizontal conductivity and harmonic mean for the vertical conductivity for instance [Renard and De Marsily, 1997].

As one can see, cross-stratifications are present in the 3-D model. The facies 2, which fills the remaining volume in the geological layers after the iterations composing facies 1 and 3 stratified deposits, represents the geological matrix. By modifying the input parameters one can update the geometry of the sedimentary structures (dimensions, degree of continuity, etc. . .) as well as some global properties such as the proportions of the different facies or their connectivity.

3.2. Comparison to Outcrops

To assess qualitatively the models generated by the proposed algorithm and in absence of an exhaustive large scale full 3-D image of the sedimentary heterogeneity within a braided system, we compare sections

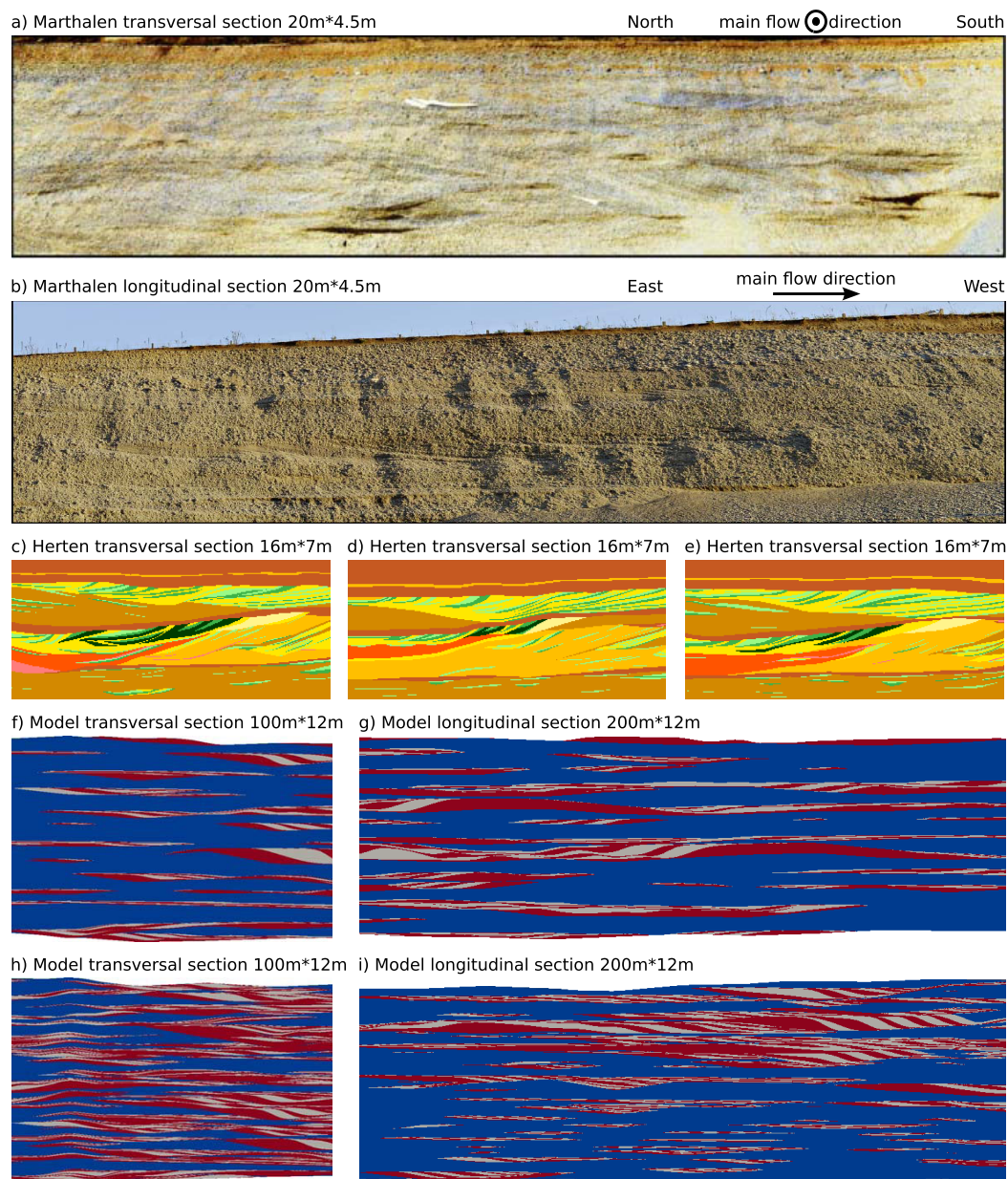


Figure 4. Comparison of model sections to field outcrops—(a and b) Photographs of braided river deposits in the Marthalen quarry (from Huber [2015]); (c–e) mapped structures in the Herten quarry, the colors represent the lithologies (from Bayer et al. [2011]); (f–i) simulated structures (the color legend is identical to the one of Figure 3).

of the generated models to field outcrops. Figures 4a and 4b, provided by Huber [2015], show sections of the Marthalen quarry in Switzerland, respectively transversal (orthogonal) and longitudinal (parallel) to the main flow direction oriented from East to West. The exposure is characterized by the superposition of several trough fills identified by clear-cut erosional lower-bounding surfaces and tangential cross-beds. The erosional lower-bounding surfaces indicate the erosional capacity of scouring. Figures 4c–4e are facies mapped along a series of outcrops at the Herten site in Southwestern Germany [Bayer et al., 2011; Comunian et al., 2011]. Though at a smaller scale, these profiles show successive cross-stratified deposits over erosional surfaces of thicker layers.

Figures 4f–4i present transversal and longitudinal sections of the models generated by the proposed algorithm. The vertical scale is exaggerated by 5. Cross-stratified deposits are clearly visible within the matrix, which is composed of successive thicker layers. This comparison between these different sections at

Table 2. Parameters Used to Study the Influence of the Aggradation Rate

Sensitive Parameter	Aggradation Rate α		Flow Power f_p		nb Iterations n	
	[0.05; 0.9]		[0.2; 9]		[3; 11]	
Curve Name	f_p Value	n Value	α Value	n Value	f_p Value	α Value
reference	5	6	0.3	6	5	0.3
low aggradation rate			0.05	6	5	0.05
high aggradation rate			0.9	6	5	0.9
low flow power	0.2	6			0.2	0.3
high flow power	9	6			9	0.3
few iterations	5	3	0.3	3		
many iterations	5	11	0.3	11		

different scales show similar patterns and underline the necessity to gather some information about characteristic length scale of the system to model, to calibrate the algorithm parameters.

3.3. Parameters and Sensitivity Analysis

The aim of this section is to provide some recommendations on how to calibrate the three main parameters of the algorithm regarding the constraints of the user—the aggradation rate α is linked to the thickness of geological units, the flow power f_p is related to the thickness of cross-stratifications and the number of iterations n is the number of cross stratifications in trough fills. To achieve this, a sensitivity analysis of these parameters on the resulting facies proportions and facies geobody connectivities is conducted hereafter. Proportions and connectivity are retained as they are important properties for underground flow and transport modeling.

As connectivity indicator we propose using the gamma connectivity measure [Renard et al., 2013]. Given an indicator variable l , its gamma-connectivity measure, Γ_l , is defined as the probability that two points belonging to the medium ($l = 1$) are connected. An indicator variable is computed for each facies. It is also possible to consider specific directions as in directional variogram computing. In what follows, we are interested in the connectivity measure along the vertical direction and in the horizontal plane.

3.3.1. Influence of the Aggradation Rate

The sensitivity analysis is performed in five different configurations. The range of values used for the aggradation parameter α as well as the values of the flow power f_p and the number of iterations n for each configuration are detailed in Table 2. The results for the sensitivity to the aggradation parameter α are illustrated in Figures 5a–5f. The black curve shows the evolution of the indicators as a function of the aggradation parameter α , for fixed reference values of the flow power f_p and of the number of iterations n . The dark gray curves show the joint effect of f_p with α . The light gray curves illustrate the joint effect of n with α .

The proportions of facies 1 and 3 decrease to the benefit of facies 2 proportion when the aggradation rate increases. This makes sense as an increase of aggradation creates thicker geological layers and there is therefore more volume for the matrix facies after the iterative deformations of the bottom layer. Low values for the flow power and number of iterations reinforce this phenomenon. The increase of facies 2 proportion implies an increase of the connectivity indicator (Figure 5e), which reaches a value almost equal to 1 (all pixels are connected) when the aggradation parameter is greater than 0.2. On the contrary, the connectivity of facies 1 and 3 are decreasing functions of α . Again, low values for the flow power and the number of iterations parameters reinforce this behavior.

Note that as facies 2 is a low permeability medium here, increasing facies 2 proportion may lead to an increase of the connectivity indicator for this facies while at the same time decreasing the aquifer global connectivity.

3.3.2. Influence of the Flow Power

In this section, the influence of the flow parameter f_p is analyzed. The range of parameter values are given in Table 2. The results are illustrated in Figures 5g–5l. Again, the black curve shows the variations of the indicators for fixed reference values of the aggradation parameter α and the number of iterations n . The dark gray curves show the joint effect of α with f_p . The light gray curves illustrate the joint effect of n with f_p .

The proportions of facies 1 and 3 increase quite rapidly at the expense of facies 2 when the flow power parameter f_p increases. This is logical since the amplitude of the iterative deformations is proportional to f_p .

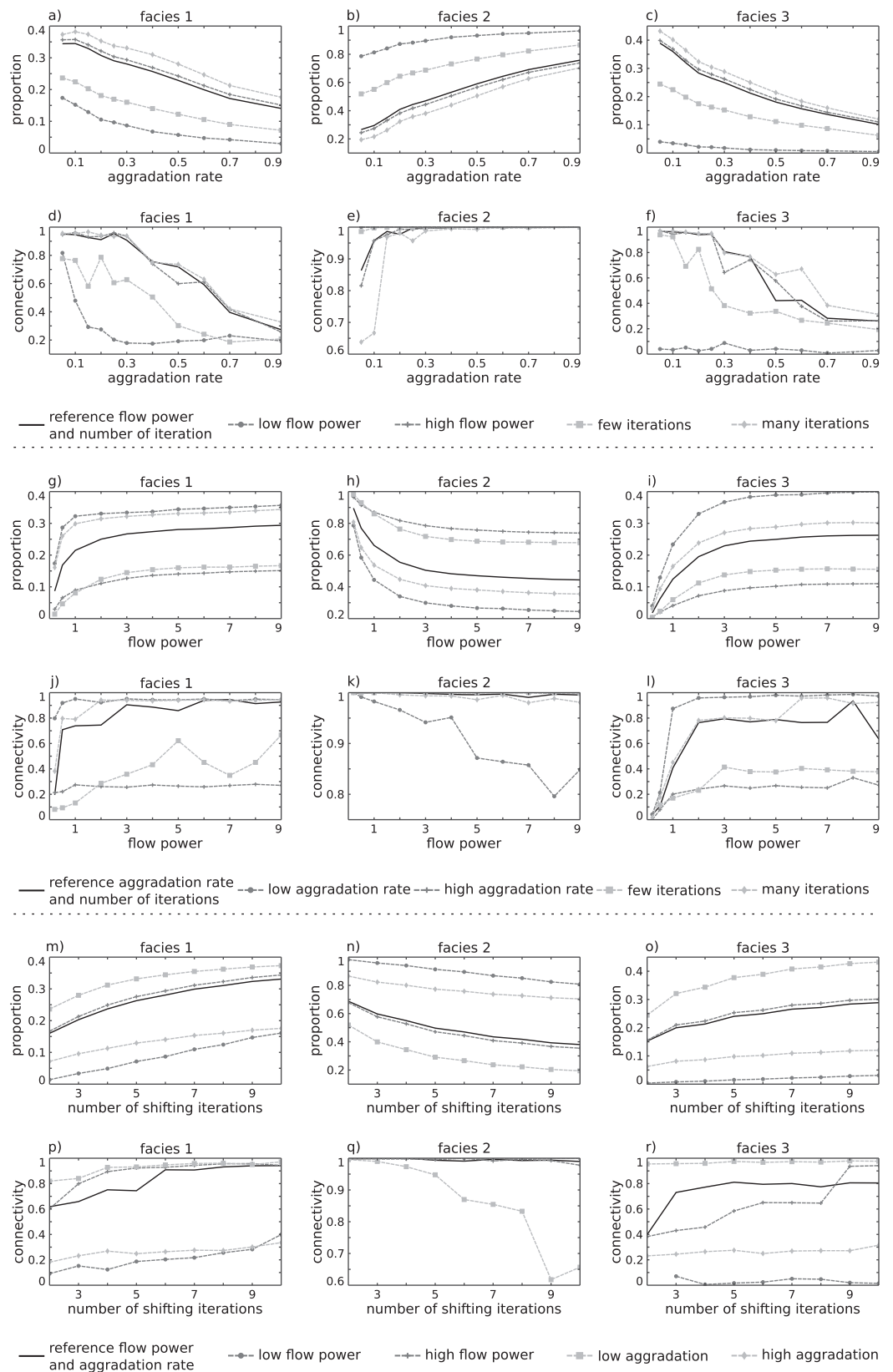


Figure 5. Sensitivity of the three main parameters on facies proportions and connectivity.

More deformation implies more cross-beds and more facies 1 and 3. Furthermore, we observe that the proportions reach a sill. This makes sense as once scours or pools are filled in the layer, the remaining volume is controlled by the aggradation rate. For facies 1 and 3, the sill of the proportion curves is lower and reached for higher f_p values with high aggradation rate value or few iterations. It is the opposite for facies 2. The connectivity of facies 1 and 3 increases with f_p . Full connectivity for facies 2 is almost constant; it decreases slightly with increasing f_p only for a low aggradation rate. The sill and range of the connectivity curves follow the same pattern as the proportion curves for high or low values of the aggradation or number of iterations parameters.

3.3.3. Influence of the Number of Iterations

The impact of the number of iterations n parameter is also assessed for different combinations of the other parameters. The range of values used are specified in Table 2. The results are illustrated in Figures 5m–5r.

Once more, the black curve shows the evolution of the indicators as a function of the number of iterations n , for fixed reference values of the flow power f_p and of the aggradation rate α . The dark gray curves show the combined effect of f_p with n . The light gray curves illustrate the joint effect of α with n .

The proportions of facies 1 and 3 increase slowly to the detriment of facies 2 when the number of shifting iterations n increases. This is not surprising as by construction, the proportions of alternative facies 1 and 3 shall increase as a function of their occurrence in the facies sequence. For facies 1 and 3, the proportion curves are lower with high aggradation rates α or with low flow power f_p values. It is the opposite for facies 2. One could expect similar sills as observed in the indicator plotted as a function of the flow power f_p . However, these sills are not reached with the range of values, because the shifting and the deformation of the topography gets smaller and smaller at each iteration. Indeed, even though the local flow is the same, the absolute value of topography gradient decreases at each iteration. The connectivity of facies 1 and 3 increases slowly with n . Full connectivity for facies 2 is almost constant; it decreases slightly with increasing n only for low aggradation rates. The connectivity curves follow the same pattern as the proportion curves regarding high or low values of the aggradation rate α or flow power f_p parameters.

3.4. Recommendations on Parameter Selection

To facilitate an intuitive understanding and selection of the parameters, it is recommended that they be adjusted in two steps because the algorithm is hierarchical with two levels. First, the user should calibrate the *main structural parameters* (Table 1), as they will influence the structural morphology of the deposit and then calibrate the *geological heterogeneity parameters* (Table 1).

The structural parameters are used to build the main geological layers. The scaling factors and the aggradation rate parameters will strongly influence the dimensions of the layers and the scours. A simple way to help calibrating these parameters is to use interpretations of ground penetrating radar (GPR) data to assess the range of the layers thickness and infer the aggradation rate. If no GPR data are available, a possibility is to rely on analog data such as outcrops. In addition, channel width, bar width and length from an active part of the braided river can be used to infer the horizontal scaling factors so that the topological characteristics of the training image match those of the braided river. This process is iterative and requires some trial and errors.

The geological heterogeneity parameters such as the flow power f_p or the number of shifting iterations n might unfortunately be more difficult to calibrate. A suggestion is to use facies proportions, which could be inferred from borehole sample, outcrop analysis, gravel pit analogs or sediment grain size distribution along the river, or a combination of these field observations and analysis. Another possibility is to measure facies thickness from boreholes or outcrop—possibly from analog sites—and compare them with boreholes or sections in the simulated depositional model to adjust the parameters.

4. Discussion and Conclusion

The pseudo-genetic algorithm presented here allows the simulation of braided-river heterogeneous deposits. Three-dimensional representations (Figure 3) and two-dimensional sections (Figure 4) of some stochastic realizations obtained with this model reveal realistic sedimentary structures such as cross-stratifications that can be observed in gravel outcrops. The method consists of two main steps: (1) generating successive DEMs using MPS with multivariate training images constituted of DEMs at different time steps of an analog

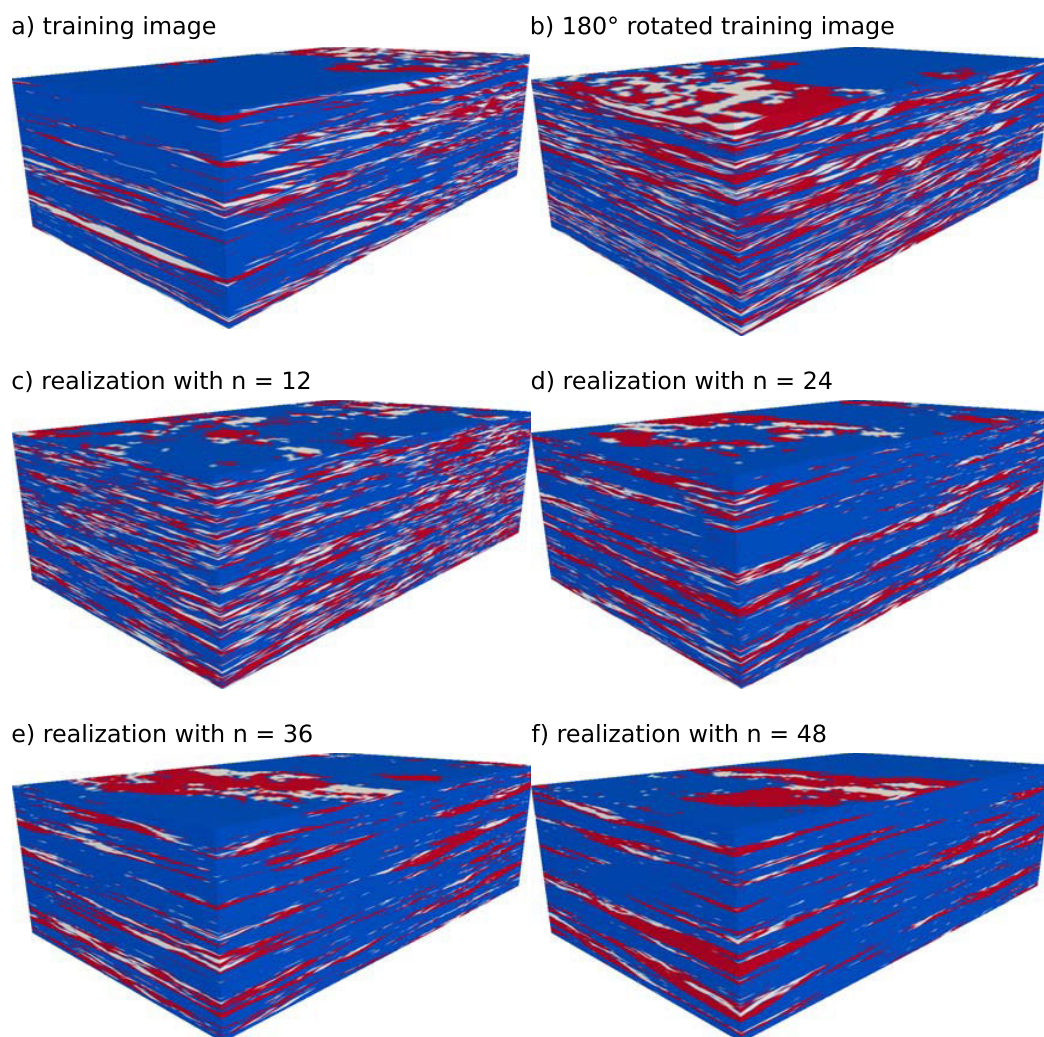


Figure 6. Examples of MPS simulations varying the number of neighbors n parameter. The scanning fraction of the training image has been set to 0.35 and the acceptance threshold to 0.05.

site; and (2) stacking these topographies to create the main geological units in a 3-D volume, and filling these units with fine-scale heterogeneity by mimicking the sediment depositional process based on an approximate flow derived from the generated topographies. One main advantage of the method is the small number (three) of influential parameters: an aggradation rate α which controls the thickness of the main geological units (erosion and deposit zones); a flow power f_p controlling the thickness of cross-stratified deposits within the main layers and related to the energy of the system; and a number of intra-layer iterations n giving the number of cross-stratified deposits.

The proposed method can be applied to generate 3-D heterogeneity by using analog data, in particular if no DEM is available for the modeling site. An advantage of the approach is that it does not require extensive field investigations as only characteristic length scales are necessary to calibrate the model, and these can be obtained by noninvasive methods such as GPR measurements or accessible outcrops. Finally, it is clearly possible to control the connectivity of the different facies by adjusting the input parameters.

However, a difficulty is that the relation between the three main parameters and the characteristic length scales at a given modeling site are not straightforward and therefore require some trial and error calibration. Furthermore, even if the resulting models seem satisfactory compared to outcrop or field observations, further work should be conducted in order to compare with other modeling approaches the ability of the resulting depositional models to predict solute and contaminant migration [Pirrot *et al.*, 2015].

Even if the method developed here does not account directly for borehole data conditioning, a simple way to accomplish this is to use the model described in this paper to construct 3-D training images. Then these images can be used in a standard multiple-point statistics (MPS) framework to model the 3-D distribution of the facies as illustrated in Figure 6. The simulations shown in this figure have been generated with the Direct Sampling algorithm [Mariethoz *et al.*, 2010] and can be directly conditioned to borehole data as it is an inherent ability of MPS implementations [Strebelle, 2002; Mariethoz *et al.*, 2010; Straubhaar *et al.*, 2013; Straubhaar and Malinverni, 2014].

Another aspect of hard conditioning to field data is to account for large geological structures inferred from GPR section interpretation for example. This means simultaneously constraining the MPS topographic simulations with the aggradation rate and there may be a high degree of uncertainty related to the interpretations. Another possibility to achieve such surfaces conditioning could be to deform the simulated geological units to fit the field data while minimizing a built-on-purpose deformation cost function. More generally, the proposed model could be used to generate prior models in an inverse framework. GPR soft conditioning could for instance be envisioned in an inversion framework based on summary statistics [Lochbühler *et al.*, 2015].

Acknowledgments

The work presented in this paper is part of the ENSEMBLE project, funded by the Swiss National Science Foundation under the contract CRSI22 1222491. The authors would like to thank Stuart Lane for having provided the Waimakariri River data set, Emanuel Huber and Peter Huggenberger for the pictures of the Marthalen outcrops, Grégoire Mariethoz and Nicolas Flipo for their constructive and motivating discussions, the reviewers and the editor for their will of clarifying and publishing the manuscript. The data supporting Figure 1 are available on request at the corresponding author or can be reproduced as described in a previous paper of the corresponding author [Pirrot *et al.*, 2014], based on the DeeSse algorithm and the Waimakariri River data set. The DeeSse algorithm is available for academic purpose on request at philippe.renard@unine.ch. A Matlab implementation of the proposed algorithm is available on request from the corresponding author.

References

- Allen, J. (1983), Studies in fluvial sedimentation: Bars, bar-complexes and sandstone sheets (low-sinuosity braided streams) in the Brownstones (L. Devonian), Welsh Borders, *Sediment. Geol.*, 33(4), 237–293.
- Anderson, M., J. Aiken, E. Webb, and D. Mickelson (1999), Sedimentology and hydrogeology of two braided stream deposits, *Sediment. Geol.*, 129(3), 187–199.
- Ashmore, P. E. (1982), Laboratory modelling of gravel braided stream morphology, *Earth Surf. Processes Landforms*, 7(3), 201–225.
- Ashmore, P. E. (1988), Bed load transport in braided gravel-bed stream models, *Earth Surf. Processes Landforms*, 13(8), 677–695.
- Ashworth, P., R. Ferguson, P. Ashmore, C. Paola, D. Powell, and K. Prestegarda (1992), Measurements in a braided river chute and lobe: 2. Sorting of bed load during entrainment, transport, and deposition, *Water Resour. Res.*, 28(7), 1887–1896.
- Ashworth, P., J. L. Best, J. O. Leddy, and G. W. Geehan (1994), *The Physical Modelling of Braided Rivers and Deposition of Fine-Grained Sediment*, John Wiley, Chichester, U. K.
- Ashworth, P. J. (1996), Mid-channel bar growth and its relationship to local flow strength and direction, *Earth Surf. Processes Landforms*, 21(2), 103–123.
- Bayer, P., P. Huggenberger, P. Renard, and A. Comunian (2011), Three-dimensional high resolution fluvio-glacial aquifer analog—Part 1: Field study, *J. Hydrol.*, 405(1), 1–9.
- Boggs, J. M., L. M. Beard, W. R. Waldrop, T. B. Stauffer, W. G. MacIntyre, and C. P. Antworth (1993), Transport of tritium and four organic compounds during a natural-gradient experiment (MADE-2), *Tech Rep. EPRI-TR-101998*, Elect. Power Res. Inst., Palo Alto, Calif.
- Brasington, J., D. Vericat, and I. Rychkov (2012), Modeling river bed morphology, roughness, and surface sedimentology using high resolution terrestrial laser scanning, *Water Resour. Res.*, 48, W11519, doi:10.1029/2012WR012223.
- Bridge, J. S., J. Alexander, R. E. Collier, R. L. Gawthorpe, and J. Jarvis (1995), Ground-penetrating radar and coring used to study the large-scale structure of point-bar deposits in three dimensions, *Sedimentology*, 42(6), 839–852.
- Cao, S., and S. Greenhalgh (1994), Finite-difference solution of the eikonal equation using an efficient, first-arrival, wavefront tracking scheme, *Geophysics*, 59(4), 632–643.
- Comunian, A., P. Renard, J. Straubhaar, and P. Bayer (2011), Three-dimensional high resolution fluvio-glacial aquifer analog—Part 2: Geostatistical modeling, *J. Hydrol.*, 405(1), 10–23.
- Coulthard, T. J., M. G. Macklin, and M. J. Kirkby (2002), A cellular model of Holocene upland river basin and alluvial fan evolution, *Earth Surf. Processes Landforms*, 27(3), 269–288.
- Dargahi, B. (2004), Three-dimensional flow modelling and sediment transport in the River Klarälven, *Earth Surf. Processes Landforms*, 29(7), 821–852.
- Davy, P., and D. Lague (2009), Fluvial erosion/transport equation of landscape evolution models revisited, *J. Geophys. Res.*, 114, F03007, doi:10.1029/2008JF001146.
- Dawson, M. (1988), Sediment size variation in a braided reach of the Sunwapta River, Alberta, Canada, *Earth Surf. Processes Landforms*, 13(7), 599–618.
- De Serres, B., A. G. Roy, P. M. Biron, and J. L. Best (1999), Three-dimensional structure of flow at a confluence of river channels with discordant beds, *Geomorphology*, 26(4), 313–335.
- Edwards, P., J. Kollmann, A. Gurnell, G. Petts, K. Tockner, and J. Ward (1999), A conceptual model of vegetation dynamics on gravel bars of a large Alpine river, *Wetlands Ecol. Manage.*, 7(3), 141–153.
- Felletti, F., R. Bersezio, and M. Giudici (2006), Geostatistical simulation and numerical upscaling, to model ground-water flow in a sandy-gravel, braided river, aquifer analogue, *J. Sediment. Res.*, 76(11), 1215–1229.
- FOEN (2009), Groundwater in Switzerland, Federal Office for the Environment. [Available at <http://www.bafu.admin.ch/grundwasser/07496/07516/index.html?lang=en>]
- Foufoula-Georgiou, E., and V. Sapozhnikov (2001), Scale invariances in the morphology and evolution of braided rivers, *Math. Geol.*, 33(3), 273–291.
- Fredsoe, J. (1978), Meandering and braiding of rivers, *J. Fluid Mech.*, 84(04), 609–624.
- Germanoski, D., and S. Schumm (1993), Changes in braided river morphology resulting from aggradation and degradation, *J. Geol.*, 101(4), 451–466.
- Glenz, D. (2013), Inverse modeling of groundwater flow in the rhône alluvial aquifer—Impact of the third rhône correction, PhD thesis, Univ. of Neuchâtel, Switzerland.
- Google-Images (2015), Saint gingolph flooding pictures. [Available at <https://www.google.ch/search?q=saint+gingolph+flooding+pictures&source=inms&tbm=isch&sa=X&ved=0CAcQAUoAWoVChMpelDINziyAIVi1ssCh0UIQM6&biw=1440&bih=776>]

- Heinz, J., S. Kleinedam, G. Teutsch, and T. Aigner (2003), Heterogeneity patterns of Quaternary glaciofluvial gravel bodies (SW-Germany): Application to hydrogeology, *Sediment. Geol.*, *158*(1), 1–23.
- Howard, A. D., M. E. Keetch, and C. L. Vincent (1970), Topological and geometrical properties of braided streams, *Water Resour. Res.*, *6*(6), 1674–1688.
- Huber, E. (2015), Incorporating sedimentological observations, hydrogeophysics and conceptual knowledge to constrain 3d numerical heterogeneity models of alluvial systems, PhD thesis, Univ. of Basel., Basel.
- Huber, E., and P. Huggenberger (2015a), Morphological perspective on the sedimentary characteristics of a coarse, braided reach: Tagliamento river (ne Italy), *Geomorphology*, *248*, 111–124.
- Huber, E., and P. Huggenberger (2015b), Subsurface flow mixing in coarse, braided river deposits, *Hydrol. Earth Syst. Sci. Discuss.*, *12*(9), 9295–9316.
- Huggenberger, P. (1993), Radar facies: Recognition of facies patterns and heterogeneities within Pleistocene rhine gravels, ne Switzerland, *Geol. Soc. Spec. Publ.*, *75*(1), 163–176.
- Huggenberger, P., and C. Regli (2006), A sedimentological model to characterize braided river deposits for hydrogeological applications, in *Braided Rivers: Process, Deposits, Ecology, and Management*, edited by H. Gregory et al., pp. 51–74, Blackwell, Oxford, U. K.
- Hundey, E., and P. Ashmore (2009), Length scale of braided river morphology, *Water Resour. Res.*, *45*, W08409, doi:10.1029/2008WR007521.
- Jerolmack, D. J., and C. Paola (2007), Complexity in a cellular model of river avulsion, *Geomorphology*, *91*(3), 259–270.
- Jones, L., and S. Schumm (2009), Causes of avulsion: An overview, in *Fluvial Sedimentology VI*, edited by N. D. Smith and J. Rogers, pp. 171–178, Wiley-Blackwell, Oxford, U. K.
- Kleinhans, M. G., and W. B. T. Brinke (2001), Accuracy of cross-channel sampled sediment transport in large sand-gravel-bed rivers, *J. Hydraul. Eng.*, *127*(4), 258–269.
- Klingbeil, R., S. Kleinedam, U. Aspiron, T. Aigner, and G. Teutsch (1999), Relating lithofacies to hydrofacies: Outcrop-based hydrogeological characterisation of Quaternary gravel deposits, *Sediment. Geol.*, *129*(3), 299–310.
- Klise, K. A., G. S. Weissmann, S. A. McKenna, E. M. Nichols, J. D. Frechette, T. F. Wawrzyniec, and V. C. Tidwell (2009), Exploring solute transport and streamline connectivity using lidar-based outcrop images and geostatistical representations of heterogeneity, *Water Resour. Res.*, *45*, W05413, doi:10.1029/2008WR007500.
- Labourdette, R., and R. R. Jones (2007), Characterization of fluvial architectural elements using a three-dimensional outcrop data set: Escanilla braided system, South-Central Pyrenees, Spain, *Geosphere*, *3*(6), 422–434.
- Lane, S., R. Westaway, and D. Hicks (2003), Estimation of erosion and deposition volumes in a large, gravel-bed, braided river using synoptic remote sensing, *Earth Surf. Processes Landforms*, *28*(3), 249–271.
- Lane, S., R. Hardy, L. Elliott, and D. Ingham (2004), Numerical modeling of flow processes over gravelly surfaces using structured grids and a numerical porosity treatment, *Water Resour. Res.*, *40*, W01302, doi:10.1029/2002WR001934.
- Leopold, L. B., M. G. Wolman, M. G. Wolman, and M. G. Wolman (1957), *River Channel Patterns: Braided, Meandering, and Straight*, U.S. Gov. Print. Off., Washington, D. C.
- Lochbühler, T., J. A. Vrugt, M. Sadegh, and N. Linde (2015), Summary statistics from training images as prior information in probabilistic inversion, *Geophys. J. Int.*, *201*, 157–171.
- Lunt, I., and J. Bridge (2004), Evolution and deposits of a gravelly braid bar, Sagavanirktok River, Alaska, *Sedimentology*, *51*(3), 415–432.
- Mariethoz, G., P. Renard, and J. Straubhaar (2010), The Direct Sampling method to perform multiple-point geostatistical simulations, *Water Resour. Res.*, *46*, W11536, doi:10.1029/2008WR007621.
- Miall, A. (1977), A review of the braided-river depositional environment, *Earth Sci. Rev.*, *13*(1), 1–62.
- Miall, A. D. (1985), Architectural-element analysis: A new method of facies analysis applied to fluvial deposits, *Earth Sci. Rev.*, *22*(4), 261–308.
- Millar, R. G. (2005), Theoretical regime equations for mobile gravel-bed rivers with stable banks, *Geomorphology*, *64*(3), 207–220.
- Murray, A., and C. Paola (1994), A cellular-model of braided rivers, *Nature*, *371*(6492), 54–57.
- Murray, A., and C. Paola (2003), Modelling the effect of vegetation on channel pattern in bedload rivers, *Earth Surf. Processes Landforms*, *28*(2), 131–143.
- Peyré, G., and L. D. Cohen (2006), Geodesic remeshing using front propagation, *Int. J. Comput. Vision*, *69*(1), 145–156.
- Pirot, G., J. Straubhaar, and P. Renard (2014), Simulation of braided river elevation model time series with multiple-point statistics, *Geomorphology*, *214*, 148–156.
- Pirot, G., P. Renard, E. Huber, J. Straubhaar, and P. Huggenberger (2015), Influence of conceptual model uncertainty on contaminant transport forecasting in braided river aquifers, *J. Hydrol.*, *531*, 124–141, doi:10.1016/j.jhydrol.2015.07.036.
- Ramanathan, R., A. Guin, R. W. Ritz, D. F. Dominic, V. L. Freedman, T. D. Scheibe, and I. A. Lunt (2010), Simulating the heterogeneity in braided channel belt deposits: 1. A geometric-based methodology and code, *Water Resour. Res.*, *46*, W04515, doi:10.1029/2009WR008111.
- Renard, P., and G. De Marsily (1997), Calculating equivalent permeability: A review, *Adv. Water Resour.*, *20*(5), 253–278.
- Renard, P., D. Allard, P. Renard, and D. Allard (2013), Connectivity metrics for subsurface flow and transport, *Adv. Water Resour.*, *51*, 168–196.
- Rodgers, P., C. Soulsby, J. Petry, I. Malcolm, C. Gibbins, and S. Dunn (2004), Groundwater–surface-water interactions in a braided river: A tracer-based assessment, *Hydrol. Processes*, *18*(7), 1315–1332.
- Rust, B. R. (1972), Structure and process in a braided river, *Sedimentology*, *18*(3–4), 221–245.
- Salamon, P., D. Fernández-García, and J. Gómez-Hernández (2007), Modeling tracer transport at the MADE site: The importance of heterogeneity, *Water Resour. Res.*, *43*, W08404, doi:10.1029/2006WR005522.
- Sambrook Smith, G., J. Best, P. Ashworth, S. Lane, N. Parker, I. Lunt, R. Thomas, and C. Simpson (2010), Can we distinguish flood frequency and magnitude in the sedimentological record of rivers?, *Geology*, *38*(7), 579–582.
- Sapozhnikov, V., and E. Fofoula-Georgiou (1996), Self-affinity in braided rivers, *Water Resour. Res.*, *32*(5), 1429–1439.
- Sethian, J. A. (1996), A fast marching level set method for monotonically advancing fronts, *Proc. Natl. Acad. Sci. U. S. A.*, *93*(4), 1591–1595.
- Sethian, J. A. (1999), *Level Set Methods and Fast Marching Methods: Evolving Interfaces in Computational Geometry, Fluid Mechanics, Computer Vision, and Materials Science*, vol. 3, Cambridge Univ. Press, Cambridge, U. K.
- Siegenthaler, C., and P. Huggenberger (1993), Pleistocene rhine gravel: Deposits of a braided river system with dominant pool preservation, *Geol. Soc. Spec. Publ.*, *75*(1), 147–162.
- Straubhaar, J., and D. Malinverni (2014), Addressing conditioning data in multiple-point statistics simulation algorithms based on a multiple grid approach, *Math. Geosci.*, *46*(2), 187–204.

- Straubhaar, J., P. Renard, G. Mariethoz, R. Froidevaux, and O. Besson (2011), An improved parallel multiple-point algorithm using a list approach, *Math. Geosci.*, *43*(3), 305–328.
- Straubhaar, J., A. Walgenwitz, and P. Renard (2013), Parallel multiple-point statistics algorithm based on list and tree structures, *Math. Geosci.*, *45*(2), 131–147.
- Strebelle, S. (2002), Conditional simulation of complex geological structures using multiple-point statistics, *Math. Geol.*, *34*(1), 1–21.
- Surian, N. (2002), Downstream variation in grain size along an Alpine river: Analysis of controls and processes, *Geomorphology*, *43*(1), 137–149.
- Teles, V., J. P. Bravard, G. De Marsily, and E. Perrier (2001), Modelling of the construction of the Rhone alluvial plain since 15 000 years BP, *Sedimentology*, *48*(6), 1209–1224.
- Thomas, R., and A. P. Nicholas (2002), Simulation of braided river flow using a new cellular routing scheme, *Geomorphology*, *43*(3), 179–195.
- Thomas, R., A. P. Nicholas, and T. A. Quine (2007), Cellular modelling as a tool for interpreting historic braided river evolution, *Geomorphology*, *90*(3), 302–317.
- Van De Lageweg, W., W. Van Dijk, and M. Kleinhans (2013), Morphological and stratigraphical signature of floods in a braided gravel-bed river revealed from flume experiments, *J. Sediment. Res.*, *83*(11), 1032–1045.
- van der Nat, D., A. Schmidt, K. Tockner, P. Edwards, and J. Ward (2002), Inundation dynamics in braided floodplains: Tagliamento river, northeast Italy, *Ecosystems*, *5*(7), 0636–0647.
- Webb, E. K. (1994), Simulating the three-dimensional distribution of sediment units in braided-stream deposits, *J. Sediment. Res., Sect. B*, *64*(2), 219–231.
- Webb, E. K. (1995), Simulation of braided channel topology and topography, *Water Resour. Res.*, *31*(10), 2603–2611.
- Williams, P. F., and B. R. Rust (1969), The sedimentology of a braided river, *J. Sediment. Petrol.*, *39*(2), 649–679.